Available online at www.sciencedirect.com
SCIENCE DIRECT®
Combustion and Flame 144 (2006) 1–16
Combustion and Flame
www.elsevier.com/locate/combustflame

Spatially resolved heat release rate measurements in turbulent premixed flames

B.O. Ayoola [a], R. Balachandran [b], J.H. Frank [c], E. Mastorakos [b], C.F. Kaminski [a,*]

[a] *Department of Chemical Engineering, University of Cambridge, Cambridge, UK*
[b] *Department of Engineering, University of Cambridge, Cambridge, UK*
[c] *Combustion Research Facility, Sandia National Laboratories, USA*

Received 7 February 2005; received in revised form 7 June 2005; accepted 16 June 2005

Available online 19 August 2005

Abstract

Heat release rate is a fundamental property of great importance for the theoretical and experimental elucidation of unsteady flame behaviors such as combustion noise, combustion instabilities, and pulsed combustion. Investigations of such thermoacoustic interactions require a reliable indicator of heat release rate capable of resolving spatial structures in turbulent flames. Traditionally, heat release rate has been estimated via OH or CH radical chemiluminescence; however, chemiluminescence suffers from being a line-of-sight technique with limited capability for resolving small-scale structures. In this paper, we report spatially resolved two-dimensional measurements of a quantity closely related to heat release rate. The diagnostic technique uses simultaneous OH and CH_2O planar laser-induced fluorescence (PLIF), and the pixel-by-pixel product of the OH and CH_2O PLIF signals has previously been shown to correlate well with local heat release rates. Results from this diagnostic technique, which we refer to as heat release rate imaging (HR imaging), are compared with traditional OH chemiluminescence measurements in several flames. Studies were performed in lean premixed ethylene flames stabilized between opposed jets and with a bluff body. Correlations between bulk strain rates and local heat release rates were obtained and the effects of curvature on heat release rate were investigated. The results show that the heat release rate tends to increase with increasing negative curvature for the flames investigated for which Lewis numbers are greater than unity. This correlation becomes more pronounced as the flame gets closer to global extinction.

Keywords: Heat release rate imaging; Simultaneous OH and CH_2O PLIF; OH chemiluminescence; Turbulent premixed flames; Flame front curvature

1. Introduction

Chemiluminescence measurements are widely used in estimating global heat release rates in hydrocarbon flames [1]. The simplicity of the experimental implementation, combined with the flexibility of species selectivity, makes chemiluminescence a very useful diagnostic in modern combustion research. Chemiluminescence is the radiative emission given off by chemically excited reactive species (denoted by "*") and serves as a good indicator of global heat release rate in premixed hydrocarbon flames. The

* Corresponding author.
E-mail address: cfk23@cam.ac.uk (C.F. Kaminski).

0010-2180/$ – see front matter
doi:10.1016/j.combustflame.2005.06.005

intensity of the chemiluminescent radiation varies linearly with fuel flow rate at a constant equivalence ratio [2]. As a result, chemiluminescence has been extensively used to study different unsteady combustion phenomena. Haber et al. [3] used OH^* and CH^* to develop a measure of unsteady heat release rate in a laminar Bunsen flame. Lieuwen and Neumeier [4] and Bloxsidge et al. [5] have reported on the use of CH^* to obtain transfer functions relating heat release and pressure fluctuations in an unsteady combustor. Other chemiluminescent species have been considered as indicators of heat release, such as C_2 and CO_2 [6,7]. However, chemiluminescence suffers from being a line-of-sight technique with limited spatial resolution; hence, small-scale structures and local heat release rates cannot be resolved. Chemiluminescence is inadequate for studying the detailed interactions between reaction layers and turbulent flow structures, which can result in localized variations in strain and heat loss, as well as extinction.

In order to resolve spatial structures in unsteady combustion, planar laser-induced fluorescence (PLIF) methods are often employed. Here, fluorescence is captured from the intersection volume of a thin laser sheet in a flame, and small-scale structures are preserved in the resulting signal images. The technique is species-selective and sensitive, with signal levels proportional to the relative concentrations of the excited species. One species that has been imaged using PLIF is the formyl radical (HCO), which has the particular advantage of being an excellent indicator of heat release rate in steady and unsteady hydrocarbon flames [7]. The production rate of the formyl radical provides a good measure of heat release because HCO is the final step along one of the major pathways to the production of CO, and a large fraction of reactions proceed along this route. Furthermore, a significant source of HCO production involves reactions with CH_2O, and CH_2O is in turn produced by one of the main heat release reactions, $CH_3 + O \rightarrow CH_2O + H$. Since the removal rate of the highly reactive formyl radical is significantly faster than its production rate, the HCO concentration is directly proportional to its production rate [7]. As a result, the HCO concentration correlates directly with the heat release rate. However, the direct PLIF measurement of HCO is very difficult due to its short fluorescence lifetime, low fluorescence quantum yield, and relatively low concentrations. An alternative approach uses the product of simultaneous OH and CH_2O PLIF measurements to obtain a signal that correlates with HCO production rate. The spectroscopic methodology of this imaging technique has been described and demonstrated by Paul and Najm [8] in a N_2-diluted premixed laminar V-flame perturbed by a vortex. Vagelopoulos and Frank [9] demonstrated the technique in undiluted premixed counterflow flames for rich and lean equivalence ratios with a range of strain rates. Both of these studies reported good correlations between heat release rates predicted from laminar flame calculations and those measured using OH and CH_2O PLIF images. Fayoux et al. [10] also report good correlations between their numerical results and heat release rate profiles measured using OH and CH_2O PLIF images in a laminar counterflow premixed flame. Böckle et al. [11] have also performed demonstration experiments in premixed swirl flames.

In this paper, we present simultaneous OH/CH_2O PLIF measurements in turbulent lean premixed flames. We compare temporally resolved and spatially averaged HR results with OH^* measurements and investigate the effects of bulk strain rates and flame curvature on the heat release rates. Experiments were performed in a turbulent premixed counterflow flame, in which bulk strain rates could be varied, and also in an acoustically forced bluff-body stabilized flame, which could be operated with and without swirl. Observed flame perturbations were the result of inlet velocity fluctuations, turbulence and swirl. These infractions on the flame front typify the conditions in industrial combustors subject to unsteady behaviors such as combustion noise, combustion induced instabilities and pulsed combustion. The bluff-body stabilized combustor investigated in this work was designed to simulate the instability phenomenon that occurs in industrial lean premixed (LP) combustors. These instabilities result from constructive interference between inlet velocity fluctuations and heat released from the flame, and they can be initiated by small variations in equivalence ratio. These variations cause corresponding fluctuations in heat release rate and consequently in gas density. The associated pressure fluctuations in the LP combustor can couple to an acoustic resonance in the combustor such that the amplitude of instabilities can either grow or decay depending on the phase of the pressure fluctuations with respect to the heat release fluctuations [4,12]. The current work is part of a wider effort to enhance our understanding of and predictive capabilities for these phenomena [13,14].

The outline of the paper is as follows. First, the implementation of the imaging technique and the process of analyzing the heat release images and chemiluminescence images are discussed. This is followed with a presentation of results from the bluff-body stabilized flame and from the counterflow flame, with an emphasis on the comparison of heat release rates obtained with OH^* chemiluminescence and with the simultaneous OH and CH_2O PLIF imaging technique. The correlation of heat release rate with curvature is then presented for the different flames investigated.

2. Experimental methods

2.1. Heat release rate imaging

In recent computational studies of steady and unsteady hydrocarbon flames, the concentration of HCO has been found to correlate well with heat release rate [7]. However, HCO is difficult to image with LIF because its accessible electronic transitions are predissociative [15]. The fluorescence signals are also strongly quenched, all resulting in very short excited-state lifetimes. In spite of these difficulties, measurements of HCO concentrations have been made by several researchers including Jeffries et al. [16] and Najm et al. [7]. The latter group reported peak signal-to-noise ratios of less than 2:1 on 100-shot averages of HCO PLIF images. As a result, the technique is only applicable in steady or periodically forced laminar flames but probably not in turbulent flames.

An alternative technique for measuring local heat release rates uses simultaneous PLIF images of OH and CH_2O [8,9]. These two species react to form the majority of HCO in hydrocarbon flames via the reaction

$$CH_2O + OH \rightarrow HCO + H_2O. \quad (1)$$

The forward rate of this reaction is $k(T)[CH_2O][OH]$, where k is the rate constant, T is temperature, and "[ ]" denote number densities. The LIF signals are related to species densities with a dependence on the local composition and temperature T that results from variations in the collisional quenching rates and Boltzmann population fraction. The product of simultaneously recorded LIF signals of CH_2O and OH can therefore be expressed as

$$(CH_2O \text{ LIF})(OH \text{ LIF}) = f(T)[CH_2O][OH], \quad (2)$$

where $f(T)$ represents the combined temperature dependence of the CH_2O and OH LIF signals. At a constant ϕ, and over a limited range of T, it is possible to select transition lines such that $f(T)$ is proportional to the forward rate constant $k(T)$ of the reaction in Eq. (1) [8]. As a result, the product of the LIF signals is proportional to the reaction rate. We selected overlapping transitions near the bandhead of the $\tilde{A}^1A_2$–$\tilde{X}^1A_1 4_0^1$ system near 353 nm for CH_2O and the $Q_1(6)$ transition in the $A^2\Sigma^+$–$X^2\Pi(1,0)$ band near 283 nm for OH. Numerical simulations were used to test the validity of the reaction rate imaging scheme for these transitions. The temperature dependences of $k(T)$ and $f(T)$ were computed using results of a laminar flame calculation for a freely propagating lean ($\phi = 0.6$) ethylene/air flame. Fig. 1 shows $k(T)$ and $f(T)$ normalized by the respective values at 1350 K. The rate constant is proportional to $T^{0.89}\exp(-204.5/T)$ [19]. The temperature- and species-dependent quenching cross sections for OH are reported in the literature [20,21], but detailed quenching data are currently not available for CH_2O. For the simulations, we assume two simplistic models of CH_2O quenching. The first model assumes that quenching cross sections are constant across the temperature range of interest. In the second model, a $1/\sqrt{T}$ dependence is assumed. The simulations indicate a good correlation between $k(T)$ and $f(T)$ for temperatures between 900 and 1500 K, which is the temperature range of significant overlap between the CH_2O and OH concentration profiles. For the two CH_2O quenching models considered here, there is little sensitivity to the functional dependence of the quenching cross sections on T. The relatively narrow range of temperatures in the region of overlap for CH_2O and OH reduces the sensitivity of the HR diagnostic to variations in $f(T)$. Further simulations in ethylene/air flames indicate that the product of the CH_2O-LIF and OH-LIF signals is primarily dependent on the CH_2O and OH concentration profiles and is only moderately sensitive to variations in $f(T)$. The results of our simulations add confidence to the validity of the technique, which was initially demonstrated in rich N_2-diluted methane flames [7]. We expect the technique to be valid for a wide range of strain rates. Law et al. [22] investigated planar premixed hydrocarbon flames with Lewis number Le > 1 and reported that flame temperature profiles are relatively insensitive to variations in strain rate.

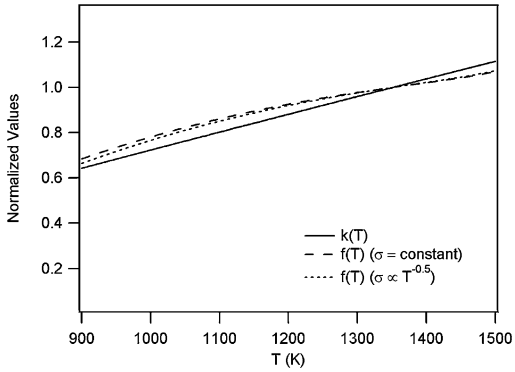

Fig. 1. Calculated profiles of the rate constant, $k(T)$, and $f(T)$, the combined temperature dependence of the CH_2O and OH-LIF signals assuming two different temperature dependencies of the quenching cross sections for CH_2O LIF. The curves are normalized by their respective values at $T = 1350$ K.

In this paper, the HR imaging technique has been used to investigate fully premixed ethylene/air flames. A similar methodology was employed by Rehm and Paul [17] and Frank et al. [18], who used simultaneous CO and OH PLIF imaging to determine a quantity

that is proportional to the forward rate of the reaction $CO + OH \rightarrow CO_2 + H$.

2.2. OH chemiluminescence imaging

Chemiluminescence is radiative emission given off by chemically excited reactive species and is extensively used as an indicator of global heat release rate in premixed hydrocarbon flames. The strongest chemiluminescence emitters in lean hydrocarbon combustion are OH^*, CH^*, and CO_2^*, and all have been used as indicators of global heat release rate and their relative merits discussed [6]. For OH^*, which was used in the present study, the peak of the $A^2\Sigma$ emission occurs at 310 ± 10 nm; hence, OH^* can be collected using UV-sensitive CCD cameras. Our measurements of OH^* include a small contribution from CO_2^* (∼10%) because CO_2^* has a broadband emission spectrum extending from 350 to 600 nm; however, the effect of this on OH^* signals is significantly reduced by the narrow-band collection of the OH^* chemiluminescence signals.

2.3. Burners

Heat release rate measurements using OH, CH_2O, and OH^* were made in counterflow and bluff-body stabilized flames. This section describes the burners, flame configurations, and diagnostic apparatus and the process of analyzing the fluorescence and chemiluminescence images. In subsequent sections, heat release rates measured with the PLIF technique will be denoted by "HR."

2.3.1. Counterflow combustor

Counterflow flames are used extensively in the verification and development of models for turbulent reacting flows [23,24]. Experimental measurements and computation of flow-field properties such as velocity and strain and their effect on the flame have been performed by a number of researchers [24–28]. Lindstedt et al. [25] used particle image velocimetry to determine planar strain rates and employed moment closure and Reynolds stress closure to model such flames numerically. Measurements of OH^* and CH^* have also been made in natural gas counterflow flames for the development of a chemiluminescence sensor as a measure of equivalence ratio [28].

The combustor used in this work consisted of two 25-mm-diameter opposing nozzles, each surrounded by a concentric tube for an external co-flow of N_2. Flow straighteners and turbulence grids were inserted into the nozzles to ensure that the turbulent velocity profiles across the outlets were uniform; the combustor is similar to that described by Mastorakos et al. [26]. The nozzles were mounted 35 mm apart

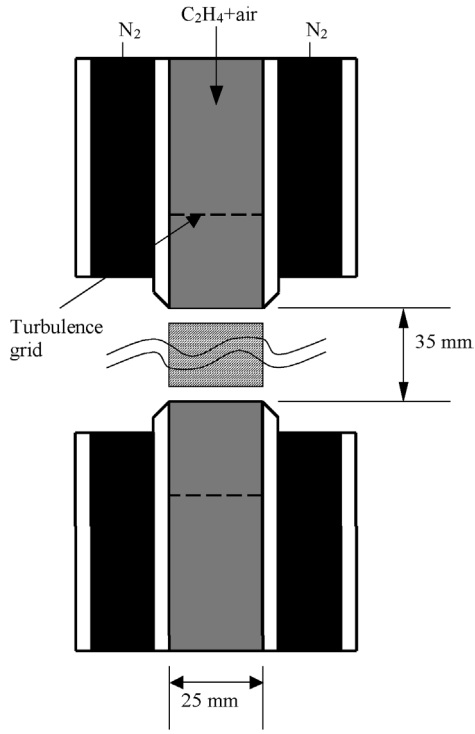

Fig. 2. Schematic of the counterflow combustor.

and fuel and air supplied using calibrated mass flow controllers. The flame was stabilized between opposed jets of premixed C_2H_4 and air at the same equivalence ratios, ranging from 0.5 to 0.7 (Le > 1). Bulk flow velocities were between 2 and 4 m/s. The latter condition resulted in flames burning close to the extinction limit. A schematic representation of the counterflow combustor is shown in Fig. 2. Both HR and OH^* measurements were taken for these conditions, with the emphasis on the investigation of the effects of the heat release rate and flame structure on increasing bulk strain rates, S_b, defined as

$$S_b = \frac{2U_b}{2D}, \tag{3}$$

where U_b is the bulk velocity from each nozzle and $2D$ is the separation between the two nozzles [28].

2.3.2. Bluff-body combustor

The 10-kW laboratory-scale bluff-body stabilized combustor was designed to model instability phenomena of the type that occur in industrial lean premixed (LP) combustors. In order to mimic such instabilities in a simple, well-controlled system, velocity fluctuations were imposed on the bluff-body flame using two acoustic drivers mounted diametrically opposite each other on the circumference of the burner plenum [13]. Measurements of HR and OH^* were carried out with the combustor operating on premixed C_2H_4 and air at

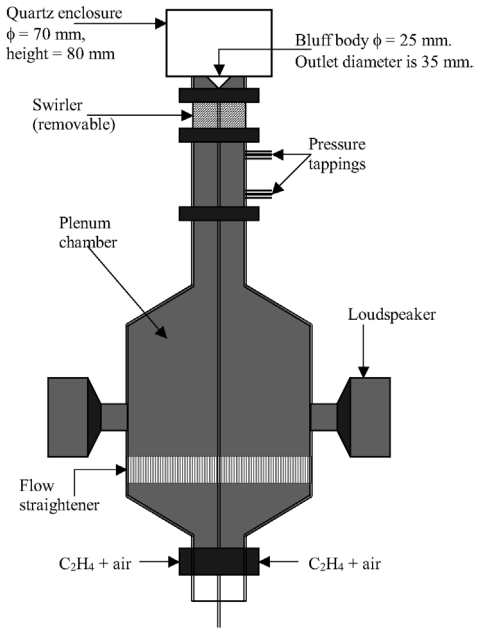

Fig. 3. Schematic of the enclosed bluff-body stabilized combustor.

Table 1
Summary of the operating conditions for the different flames investigated in the bluff-body stabilized ethylene flames

Flame no.	Forcing freq., Hz	ϕ	Swirl no.	Axial vel., m/s	Reynolds no., Re
Flame 1	0	0.60	0	9.7	19,000
Flame 2	160	0.60	0	9.7	19,000
Flame 3	0	0.45	0	15.7	29,000
Flame 4	0	0.45	0.7	9.7	19,000

equivalence ratios between 0.5 and 0.7 (Le > 1). The flame is enclosed in a quartz tube to ensure that there is no recirculation of fresh air, which would cause local variations in equivalence ratio. A schematic representation of the combustor is shown in Fig. 3.

In this paper, heat release rate measurements were made for four different bluff-body stabilized flame configurations described in Table 1. In the table, flame 1 and flame 2 refer to unforced and acoustically forced flames both at an equivalence ratio of 0.6 and a bulk velocity of 9.7 m/s. Flame 3 describes a leaner flame at an equivalence ratio of 0.45 and a bulk velocity of 15.6 m/s, while flame 4 also describes a leaner flame at a bulk velocity of 9.7 m/s and a geometric swirl number of 0.7; flame 3 and flame 4 both describe flame conditions very close to global extinction. Measurements were made with and without swirl to investigate the effect of high turbulence generated by the swirl with the flame close to global extinction.

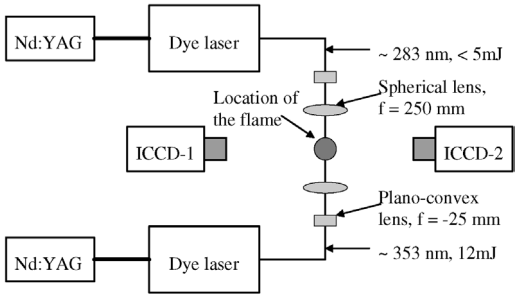

Fig. 4. Schematic of the laser imaging facility.

2.4. Diagnostic apparatus

The laser system for imaging OH and CH_2O consisted of two Nd:YAG lasers (Continuum Surelite), two dye lasers (Sirah Cobra-Stretch), and two high-resolution double-exposure ICCD cameras (Lavision Nanostar). The camera for imaging OH PLIF was fitted with a UV f/4.5 camera lens (Nikkor) equipped with UG 11 and WG 305 filters (Comar). The CH_2O camera was fitted with an f/1.2 camera lens (Nikkor) and GG 375 and SP 550 filters (Comar). For spectral identification of OH and CH_2O transitions, LIF excitation scans were performed prior to the PLIF measurements. For OH LIF, the frequency-doubled output from one dye laser was tuned near 283 nm to excite the $Q_1(6)$ line in the $A^2\Sigma^+$–$X^2\Pi(1,0)$ band. The frequency-doubled output from the second dye laser was tuned to pump the peak of overlapping transitions in the $\tilde{A}^1A_2$–$\tilde{X}^1A_1 4_0^1$ band of CH_2O near 353.17 nm. The laser beams (linewidth of 0.12 cm^{-1}) were expanded into sheets 50 mm high and 100 μm thick, using cylindrical planoconvex lenses with focal lengths of 25 mm and spherical lenses with focal lengths of 250 mm. Pulse energies of 15 mJ were available from the dye lasers at the different wavelengths, but the beams were spatially filtered and less than 5 mJ was used for the OH PLIF measurements and 12 mJ for the CH_2O measurements. This was done to ensure that the fluorescence signals were not saturated and linearly proportional to the concentrations of probed species. A schematic representation of the setup is shown in Fig. 4.

The ICCDs were each capable of acquiring two images in rapid succession. This enabled the measurement of OH PLIF shortly followed by an OH^* emission measurement on the same camera. To achieve this, the camera intensifiers were gated to open for 350 ns for the PLIF measurements and 50 μs for OH^*. A delay of 500 ns was set between the CH_2O and OH laser pulses to avoid potential interferences between the laser pulses and cameras. At the given bulk velocities and with the spatial resolution of the optical setup, the chosen delay of 500 ns between the pulses ren-

dered the PLIF measurements virtually instantaneous on flow timescales.

2.5. Image analysis

2.5.1. Fluorescence image analysis

The raw PLIF images were postprocessed before product images were calculated to obtain heat release information. First, a background image, measured in the absence of the flame, was subtracted from the fluorescence images. Second, the images were corrected for laser sheet inhomogeneities. This was done by dividing the instantaneous OH and CH_2O images by the average beam profiles of the exciting lasers. The beam profiles for each dye laser were measured prior to flame measurements in a homogeneous vapor of air-diluted biacetyl (for CH_2O) and acetone (for OH). Finally, both PLIF images were aligned with each other on a pixel-by-pixel basis. The alignment is crucial to the success of this imaging technique because of the small spatial scales of reacting layers in the flame. This alignment process was performed in several stages. First, a target image (grid pattern) was aligned in the measurement plane, defined by the laser sheets and in the view of both cameras. Second, the coordinates of several reference points on the target image, captured by the CH_2O camera, were recorded as anchor points. The target was then imaged with the OH camera. The image was mirrored and the corresponding coordinates of the same reference points were identified. Third, a transformation matrix relating the two sets of coordinates was calculated and used to map the OH images into the coordinate system of the CH_2O image. This image processing technique is similar to that employed in particle image velocimetry and its precision is in the subpixel range [29]. The corrected images were then multiplied on a pixel-by-pixel basis to obtain the heat release rate images.

Both cameras had an ICCD chip size of 1280×1024 pixels and were positioned to give a spatial resolution of 0.07 mm/pixel at the measurement plane. At this high resolution, the spatial distribution of the species being probed is clearly resolved.

2.5.2. Chemiluminescence image analysis

Since chemiluminescence is a line-of-sight technique, the averaged OH^* images were deconvolved into a 2-D projection for comparison with the HR results; this deconvolution was performed using the forward Abel transform. The Abel transform algorithm reconstructs an axial projection of an axisymmetric function according to the equation

$$f(r) = -\frac{1}{\pi}\int_r^R \frac{g'(x)\,\mathrm{d}x}{\sqrt{x^2 - r^2}}, \tag{4}$$

where $g'(x)$ is the line-of-sight integrated OH^* signal and $f(r)$ is its forward Abel transform projection. Walsh et al. [30] have reported that the peak values of Abel inverted signals can be underestimated by as much as 30%, depending on the location of the signal. At the base of the bluff body, where the distribution is thinnest, the peak of the Abel inverted OH^* signal may be underestimated relative to the OH^* signal furthest from the bluff body, where the distribution is broader. In our case, the collection solid angle for the OH^* optics is 0.04 radians and the depth of field was greater than the width of the bluff-body flame. Since the collection angle is small enough to permit the assumption of parallel rays, the error introduced from diffuse signals collected outside the depth of field is minimized.

2.6. Uncertainty estimates

The major contributors to uncertainty in the measurement of heat release rate using the HR technique are the shot-to-shot variation of the laser energy and the subtle changes that occur in the laser beam profiles. The maximum deviation in energy of both laser pulses during the period of taking PLIF measurements has been estimated to be 15% of its mean value. Spatially integrated measurements of HR and OH^* were evaluated by summing the measured quantities over the entire imaged region, and the standard deviation for a 75-shot average of these spatially integrated quantities was 20%. The laser-beam profile did not vary significantly during the acquisition of 75 instantaneous images; therefore, the PLIF images were corrected by the average beam profiles, and the uncertainty introduced as a result of variations in the beam profiles was negligible.

Additional systematic uncertainties may be introduced by variations in the local LIF quenching environment. The evaluation of this error requires temperature and species dependent quenching cross sections, which are available for OH but are quite limited for CH_2O. However, we expect this error to be relatively modest, based on the simulations discussed earlier in Section 2.1.

3. Results and discussion

Chemiluminescence from flame species such as OH, CH, and CO_2 are widely used indicators of global heat release rate in the study of premixed flames. The initial focus of the present investigation was on the comparison of global HR estimates from the HR technique and the OH^* imaging. Following this comparison, we used the HR method that, in contrast to OH^*, is capable of resolving detailed flame

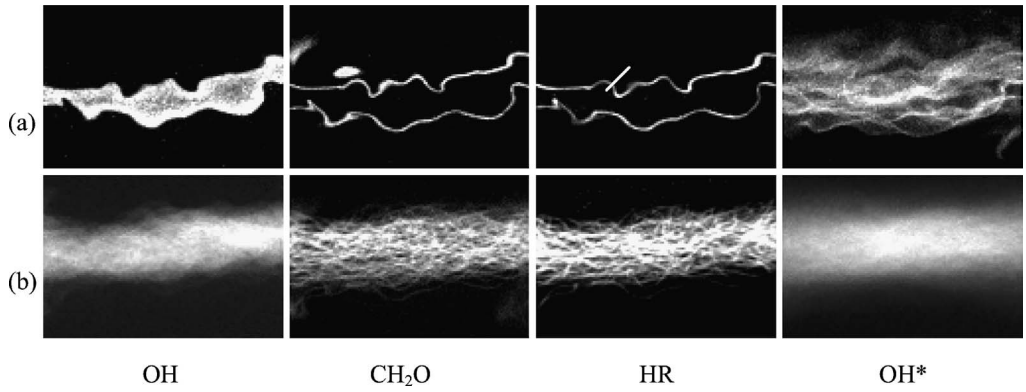

Fig. 5. (a) Instantaneous OH PLIF, CH_2O PLIF, and corresponding HR and OH^* images taken in a counterflow flame at a bulk velocity of 2.9 m/s ($S_b = 82\ s^{-1}$) with $\phi = 0.55$. The line across the flame front on the HR image indicates the position of the profiles displayed in Fig. 6. (b) An average of 75 images taken at the same bulk velocity.

structural information, to obtain correlations of local heat release rate and curvature. These measurements were performed both for the counterflow flame and for the bluff-body stabilized flame under different operating conditions. Since an aim of this paper is to compare the spatial distribution of heat release rates obtained by HR with OH^*, the results presented were normalized by their mean values.

3.1. Comparison of OH^* and HR

3.1.1. Counterflow flame

The dynamics of the counterflow combustor, by which one-dimensional flames (in the mean) are stabilized in opposed streams of reactants, enable the investigation of bulk strain rate effects by the variation of bulk flow rate (Eq. (3)). Hence, measurements of heat release rate with HR and OH^* were taken at different bulk flow rates in the premixed counterflow flame.

Fig. 5 displays simultaneous OH^*, OH PLIF, and CH_2O PLIF measurements from the shaded region of schematic diagram shown in Fig. 2. The pixel size was 0.07 mm/pixel on all measurements shown. All HR images were evaluated from single-shot PLIF measurements of OH and CH_2O before any averaging was performed. Fig. 5a shows a set of instantaneous OH PLIF, CH_2O PLIF, and OH^* measurements with the corresponding HR image taken at a bulk velocity of 2.9 m/s. Fig. 5b shows an average of 75 images for the same conditions. The Abel reconstruction was not performed on the average OH^* image shown in Fig. 5b.

The OH PLIF image shows the distribution of OH radicals in the confined postflame region between the two flames. An isolated packed of CH_2O is observed in the preheat region of the flame, indicative of cool temperature chemistry. There is no corresponding feature in the OH PLIF image, and thus no significant heat release is taking place. Formaldehyde is formed in the preheat region at relatively low temperatures (1000 K) because it is central to alternative low-temperature chemical pathways of fuel oxidation in lean hydrocarbon flames [31]. From the instantaneous HR images, we observe that the heat release rate varies along the flame front as it is affected by strain, curvature, and turbulence. The flame front is 0.5 mm thick as it is marked by the region of overlap between OH and CH_2O radicals. This can clearly be seen in Fig. 6, which shows instantaneous profiles of OH, CH_2O, and HR across the instantaneous flame front at the position marked on the HR image shown in Fig. 5.

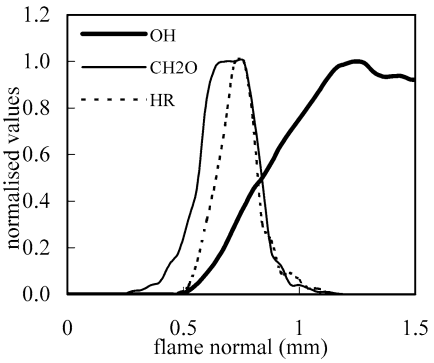

Fig. 6. Normalized profiles of OH, CH_2O, and HR taken across the flame along the line indicated on the HR image in Fig. 5a.

From the averaged heat release rate images, the spatial average, Q_{av} (average intensity of all pixels in the image), for HR and OH^* was evaluated as follows,

$$Q_{av} = \frac{\sum I_{x,y}}{n}, \tag{5}$$

where $I_{x,y}$ is the intensity at every pixel and n is the number of pixels. Fig. 7 shows the variation of Q_{av}

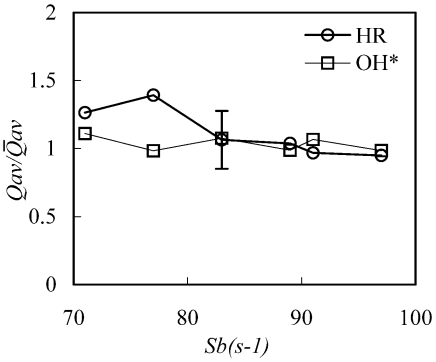

Fig. 7. Normalized profiles of HR and OH* with increasing bulk strain rate, S_b.

for HR and OH* (20% uncertainty in both quantities) with increasing bulk strain, S_b ($\bar{Q}_{av}$ is the average over all bulk strain rates). The normalized profiles of HR and OH* in the counterflow flame seem to indicate similar trends of slightly decreasing heat release rates with increasing bulk strain as was also reported by Hardalupas et al. [28]. However, with the stated uncertainties our measurements do not provide conclusive evidence for this trend. Fig. 8 shows instantaneous images of OH, CH_2O, HR, and OH*. The images show that the upper and lower flame fronts merged at the edge of an extinguished region with a bulk strain rate of 100 s^{-1}. A similar phenomenon was predicted by Bray et al. [32] and observed by Ishizuka and Law [33] and Luff et al. [34] in their study of premixed counterflow flames. This is a major advantage of using HR, as it captures spatially resolved heat release rate structures of localized phenomena such as flame merging and local extinction. A discussion of the fluctuations of heat release rate along the flame will be presented in a later section of this paper.

3.1.2. Bluff-body stabilized flame

Similar measurements were performed in the bluff-body stabilized flame over a range of equivalence ratios. Fig. 9 corresponds to flame 1 in Table 1, which is unforced (no external excitation). Fig. 9a shows a set of instantaneous and Fig. 9b shows averaged images of OH PLIF, CH_2O PLIF, and OH* and the corresponding HR images taken in flame 1 at $\phi = 0.6$. The region of the flame imaged is also shown. In the top right-hand corner of the instantaneous OH PLIF image, OH radicals can be observed on the outer side of the shear layer. Since relatively low signals of heat release rate are obtained here, it can be concluded that the majority of the OH radicals observed are a result of the recirculation of the post-combustion gases. By comparing the averaged HR and OH* images, we also observe different distributions of heat release rates. The averaged HR image shows heat release rates confined to a narrow brush

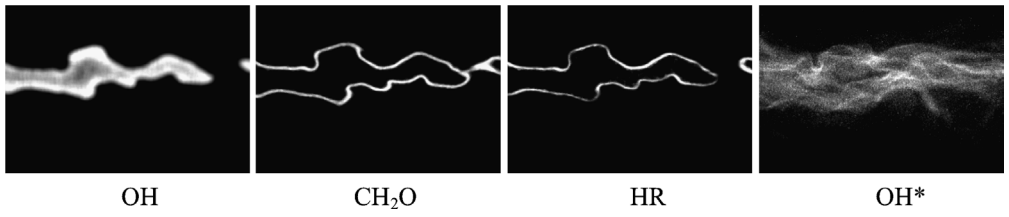

Fig. 8. Image of HR at $U_b = 3.4$ m/s and a bulk strain rate of 100 s^{-1} with the twin flames merged.

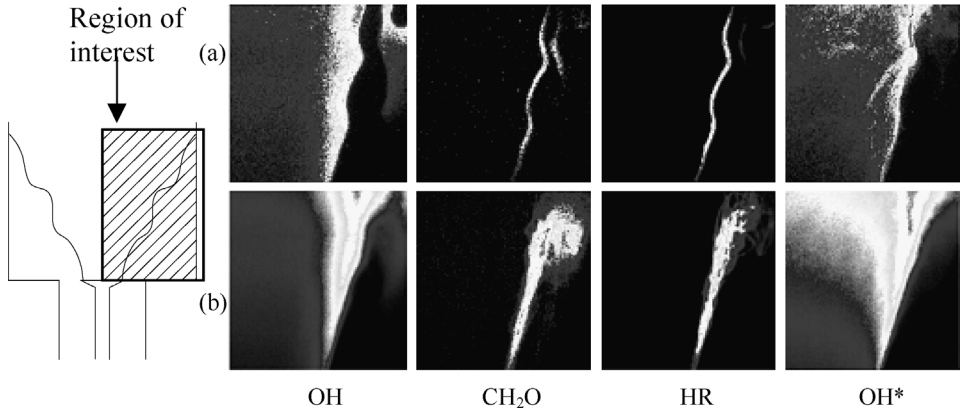

Fig. 9. (a) Images of OH PLIF, CH_2O PLIF, and corresponding HR and OH* images taken in the enclosed, unforced bluff-body stabilized flame at $\phi = 0.6$. (b) Averaged OH PLIF, CH_2O PLIF, HR, and OH*. The region imaged is also shown.

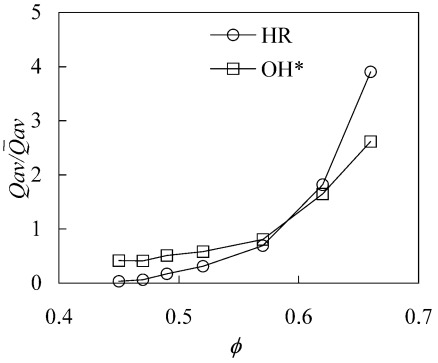

Fig. 10. Profiles of normalized HR and OH* in a bluff-body stabilized flame at different equivalence ratios.

around the flame front, while the averaged OH* image shows a much broader distribution. This is a result of the unrestricted OH* chemiluminescence species giving signals from all around the flame.

The trend of Q_{av} normalized with the overall mean of heat release rates (for all equivalence ratios considered), $\bar{Q}_{av}$, with increasing equivalence ratios is shown in Fig. 10. The maximum equivalence ratio investigated was 0.65 because at higher values, the flame flashes back at the given bulk velocity. The profiles in Fig. 10 both show similar increasing trends in heat release rate with increasing equivalence ratio. The flow close to the exit probably experiences higher strain rates than further downstream, where the turbulence length-scales increase. As a result, the flame brush downstream of the jet exit is thicker than the flame brush close to the jet exit [35]. We investigated the HR and OH* response in different parts of the flame by determining locally averaged values. The calculations presented in Fig. 10 were performed in two distinct regions of the flame front as indicated in Fig. 11a. Q_{av} was calculated for the flame at different equivalence ratios in section 1 (40 × 8 mm), 5 mm above the bluff body, and in section 2 (40 × 8 mm), 21 mm from the bluff body. The results are shown in Figs. 11b and 11c. The profiles of HR exhibit similar trends, while there are differences between the OH* profiles. There are two points of interest here. First, HR shows the same dependence on ϕ for both regions of the flame. Second, OH* rises less steeply with ϕ in section 1 (close to the bluff body) than in section 2 (further from the bluff body). This suggests that HR measures heat release rates more accurately than OH*, which seems to be more sensitive to strain and turbulence. Samaniego et al. [6] caution that OH* emission from turbulent flames should be carefully interpreted, as chemiluminescence is strongly affected by variations in strain rate and curvature. Najm et al. [7] suggest that this is due to subtle shifts in the reaction pathways of hydrocarbon combustion as a result of unsteady strain rate. Conversely, the profile of HR supports the conclusions made by Lee and Chung [23], who find that the temperature and structure of a freely propagating premixed flame is insensitive to strain rate variations. From these observations, we are led to the conclusion that HR is a good measure of heat release rate (both spatially resolved and

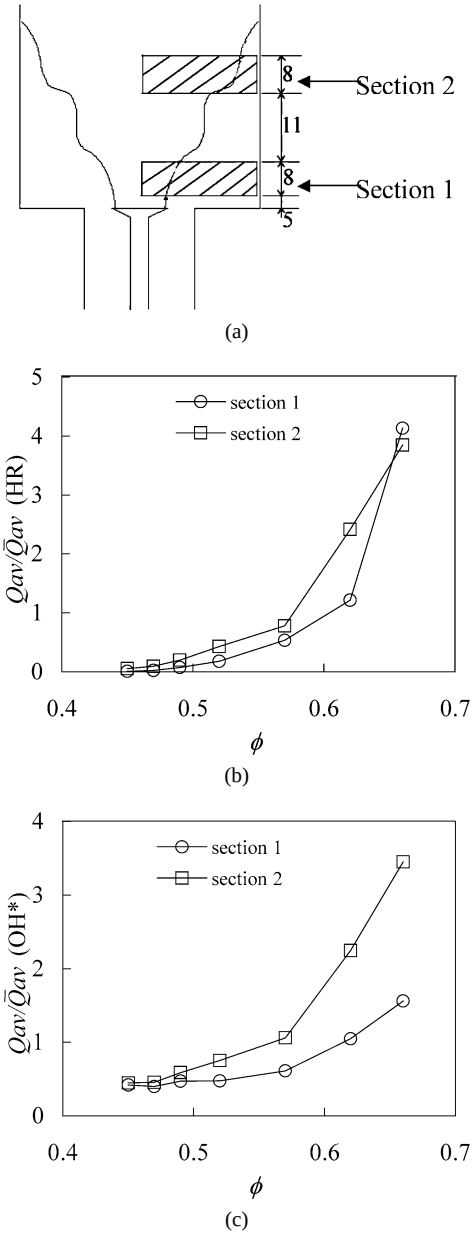

Fig. 11. (a) Schematic showing section 1 (lower) and section 2 (upper), all units in mm. (b) Profile of normalized HR close to the bluff-body (section 1) and further downstream from the bluff-body (section 2) with increasing equivalence ratios. (c) OH* of the same quantities.

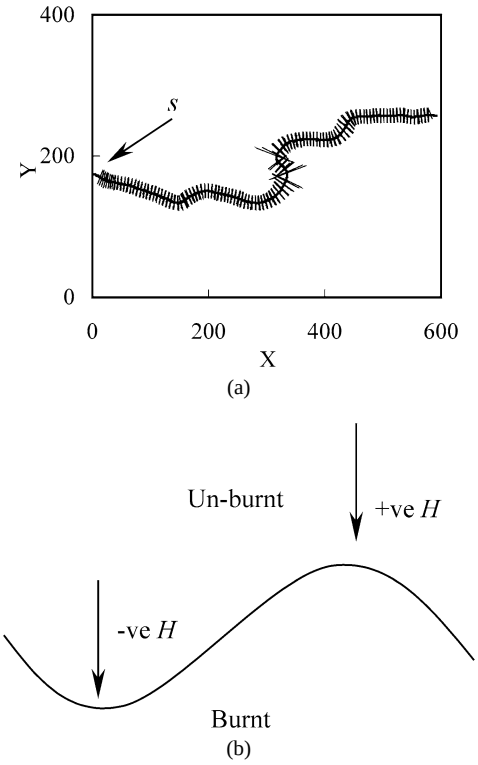

Fig. 12. (a) Schematic showing some normals along the flame front along which heat release rates were integrated and (b) definition of curvature.

global) in premixed turbulent flames. These observations indicate that the HR technique provides a more self-consistent measure of heat release rate than does OH^* chemiluminescence in these premixed turbulent flames.

3.2. Effect of curvature on heat release rate

The variation of heat release rate with curvature was investigated using the images obtained from HR in both the counterflow flame and the bluff-body stabilized flame. Such data are significant to the computational modeling of combustion because it can be used directly for the development of turbulent reactive flow models [36].

In order to obtain such correlations, the HR images were processed in two stages. First, intensities of HR images were integrated across the flame front by integrating the profile of the local heat release rates (such as in Fig. 6) along a line normal to the flame tangent at every point along the flame front. These integrated values of heat release rate data were used in heat release/curvature correlations. Fig. 12a shows a typical flame front from the counterflow flame, with evaluated flame normals across which the heat release rates were thus integrated. Second, the coordinates (x, y) of each point along the identified heat release rate contour were evaluated with respect to an origin, s (also shown in Fig. 12a), taken to be the point along the contour at which $x = 0$. With (x, y, s), the curvature, H, at every point on the flame front is calculated using [37,38]

$$H = \left[\left(\frac{\mathrm{d}^2x}{\mathrm{d}s^2}\right)^2 + \left(\frac{\mathrm{d}^2y}{\mathrm{d}s^2}\right)^2\right]^{1/2} \mathrm{mm}^{-1}. \quad (6)$$

The choice of differential width size (ds) is crucial for the calculation of curvature. In order to obtain curvatures from both small-scale and large-scale wrinkles along the flame, the value of ds used was the average crossing length of the instantaneous flame front with the heat release rate progress variable contour of 0.5. The $\bar{c}$ contour was obtained by making a contour plot of an average of binary heat release rate images (0 is unburnt and 1 is burnt). Crossing lengths are then obtained by superimposing instantaneous HR images over $\bar{c}$ = 0.5 and calculating the average distance along the flame front for which the contour is crossed by the instantaneous flame contour. The average crossing lengths thus obtained are 7 mm for the counterflow flame, 5 mm for flame 1 and flame 2 in the bluff-body stabilized flame, and 4 mm for flame 3 and flame 4. These values are inserted into Eq. (6) and H is calculated. Crossing lengths are a statistical characteristic of any flame and are dependent on the degree of flame wrinkling; hence, they are a function of turbulence and are important in the study and modeling of turbulent combustion [39,40].

With the radius of curvature on the reactant side, positive curvature was defined as convex to the reactants; conversely, negative curvature was defined as concave to the reactants. A schematic representation of this convention is shown in Fig. 12b.

3.2.1. Counterflow flame

The pdf of curvature for the counterflow flame, analyzed for 75 HR images at bulk velocities of 2.4, 2.9, and 3.4 m/s, is shown in Fig. 13a. The profile shows a mean curvature of approximately 0 with all three profiles showing an identical spread of curvatures. The contour plots of the joint pdf of heat release rate, Q (normalized with the mean $\bar{Q}$ at $H = 0$), and curvature, from the integrated HR image, are shown for the three bulk velocities in Figs. 13b–13d. The contours show that the majority of HR was measured at a curvature close to zero with a slight increase in HR toward negative and positive curvatures. This correlation is more evident in the profile of conditionally averaged HR against curvature shown in Fig. 14. Researchers have reported that the trend in this correlation is for increased heat release rates at negative curvatures and decreased heat release rates at positive curvatures [41–43]. The correlation could be the

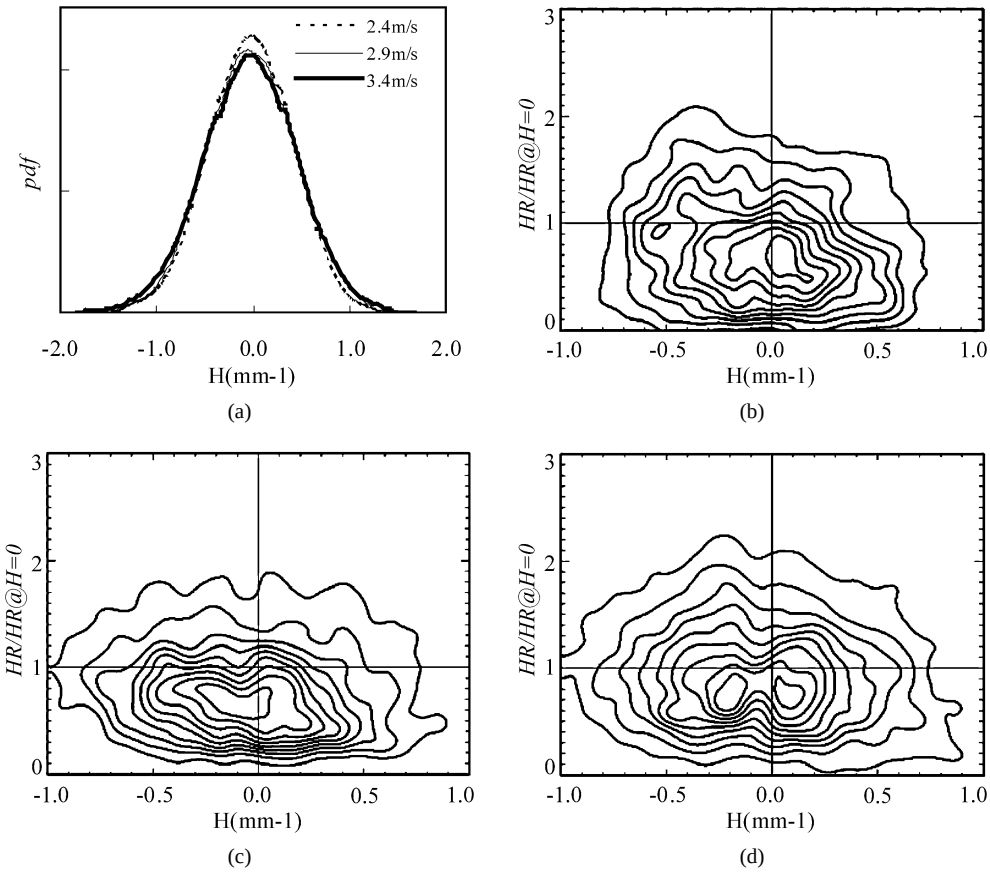

Fig. 13. (a) pdf of curvature (H) at different bulk velocities in the counterflow flame and contour plots of the joint pdf of HR and curvature at (b) 2.4, (c) 2.9, and (d) 3.4 m/s.

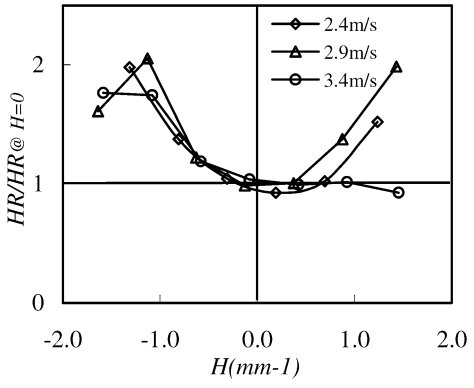

Fig. 14. Average profiles of HR against curvature for the different bulk velocities investigated in the premixed counterflow flame.

result of an increased diffusion rate of propagating radicals such as H from the reactant-side of the flame as suggested by Echekki and Chen [41] for flames with Lewis number Le > 1. At high velocities, this trend is indeed captured. At low velocities, the heat release seems to increase with positive curvature. The trend for this is not clear.

3.2.2. Bluff-body stabilized flame

In the bluff-body stabilized flame, the correlation between heat release rate and curvature is analyzed for all the flames described in Table 1. Fig. 15a shows a set of instantaneous OH PLIF, CH_2O PLIF, and OH^* with the corresponding HR image taken at in flame 2 and Fig. 15b shows an average of 75 images of the same species. The flame is acoustically forced at 160 Hz and the images are taken at a phase angle of 55° relative to the forcing signal. The images show the effects of a pair of counterrotating vortices transporting premixed reactants and wrapping the flame front. The postgas region marked with OH radicals is shown in the OH PLIF image and the preheat zone is marked in the CH_2O PLIF image. One of the vortices is filled with CH_2O, indicating the penetration of the preheat zone into the reactant mixture as the flame front, shown by HR, encircles these vortices. It is worth mentioning that the vortices are also partially visible in the OH^* images, but at much reduced

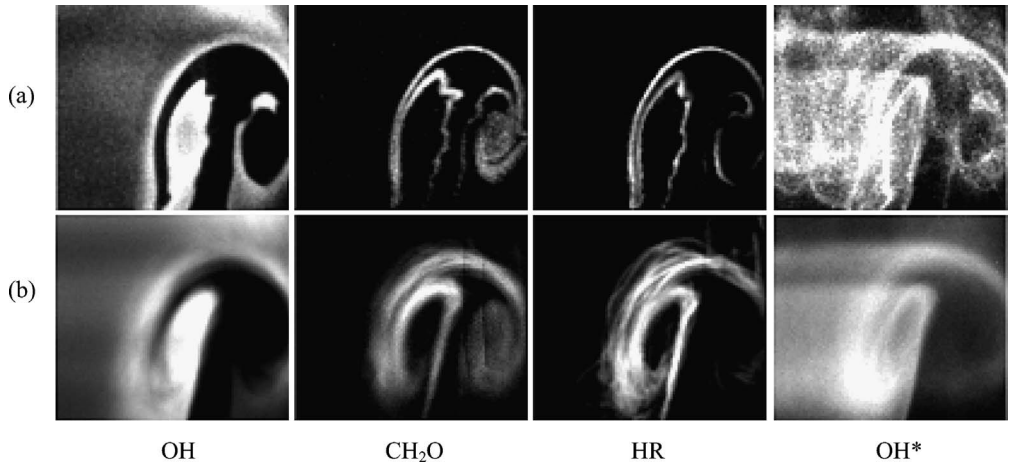

Fig. 15. (a) Instantaneous OH PLIF and CH_2O PLIF and the corresponding HR and OH^* images taken in the enclosed bluff-body stabilized flame forced at 160 Hz with $\phi = 0.6$ and axial velocity 9.7 m/s. These images were taken at a phase angle of 55° with respect to the input forcing signal. (b) Phase averaged OH PLIF, CH_2O PLIF, HR, and OH^*.

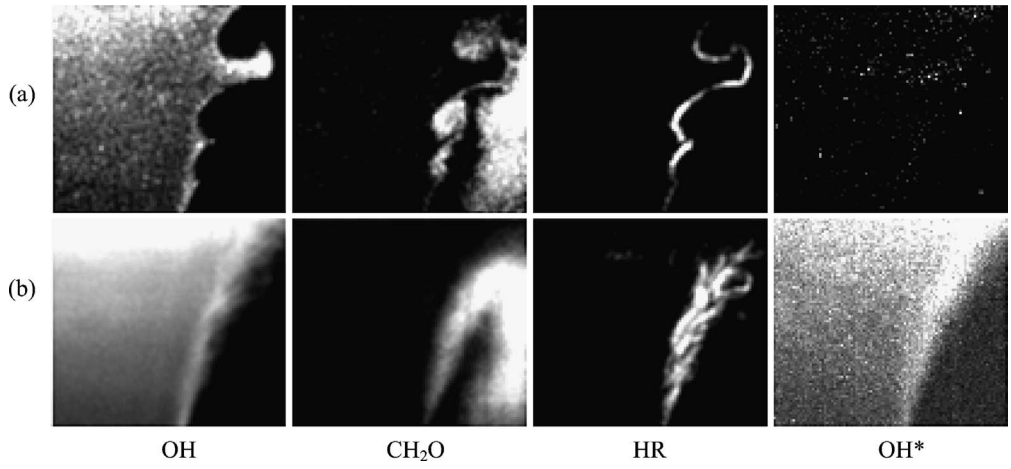

Fig. 16. (a) Instantaneous OH PLIF and CH_2O PLIF and corresponding HR and OH^* images taken in the enclosed, bluff-body stabilized flame with ϕ = 0.45 and an axial velocity of 15.6 m/s. (b) Phase-averaged OH PLIF, CH_2O PLIF, HR, and OH^*.

clarity. Similar measurements were made in flame 3 and the images are shown in Fig. 16 (bulk velocity of 15.6 m/s, $\phi = 0.45$). This flame has a bulk velocity much greater than that of flame 2 and hence is more turbulent. These conditions are close to lean blowout limits of the combustor. The flame front is highly wrinkled and has small eddies propagating along it; this is clearly seen in the CH_2O PLIF image in Fig. 16. At this equivalence ratio, the signal to noise ratio of the OH^* images is approximately 1.5:1; therefore, OH^* is only visible in the averaged image, whereas the HR still performs on a single shot basis. Similar observations can be made for flame 4 shown in Fig. 17. Here, the flame is close to global extinction and is furthermore subjected to swirl. The flame front is clearly more intermittent and wrinkled as seen in the HR image. Mixing is much more intense and the flame is shorter.

The pdf of curvature for each of these flames is shown in Fig. 18. The larger spread of curvatures from flame 1 to flame 2 is due to the acoustic forcing of the flame. As the inlet velocity is sinusoidally varied, periodic large-scale vortices are imposed on the flame front; this results in imposed curvature on the flame front as the flame wraps around the vortex. As the bulk velocity is increased from flame 1 to flame 3, the peak of the pdf decreases and the spread of curvatures increases. This trend continues to flame 4 where the flame is subjected to swirl. As the flame gets more turbulent and is closer to lean blowout (flame 1 to flame 4), the peak of the pdf decreases and moves toward negative curvatures while the spread of cur-

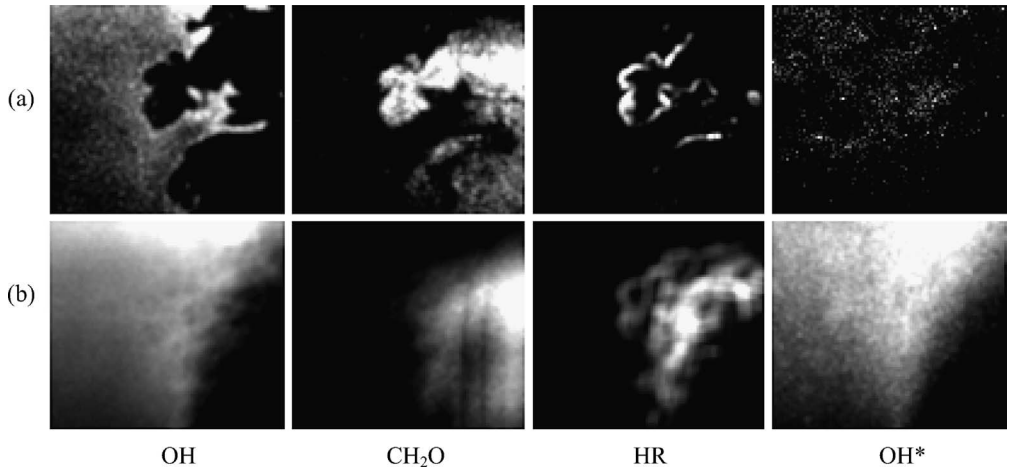

Fig. 17. (a) Instantaneous OH PLIF and CH_2O PLIF and the corresponding HR and OH^* images taken in the enclosed, bluff-body stabilized flame with $\phi = 0.45$, axial velocity of 9.7 m/s and a geometric swirl number of 0.7. (b) Phase-averaged OH PLIF, CH_2O PLIF, HR, and OH^*.

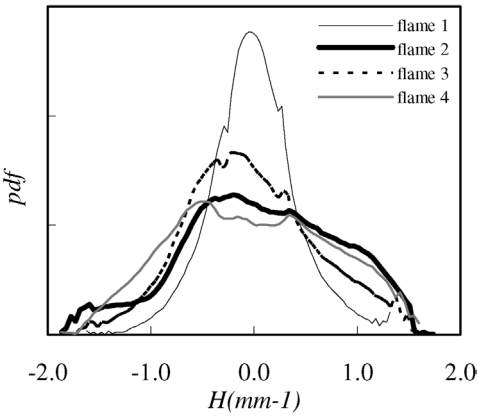

Fig. 18. pdf of curvature calculated from the bluff-body stabilized flames described in Table 1. Flame 1, unforced flame; flame 2, forced flame; flame 3, high velocity and close to extinction; and flame 4, high swirl and close to extinction.

vatures increases. The trend of increasing widths of the curvature pdf with turbulence intensity is consistent with the DNS results of Gashi et al. [44].

The contour plot of the joint pdf of heat release rate and curvature for each flame is shown in Fig. 19. In all the cases, the contours show higher HR with negative curvatures, compared with HR at positive curvatures. This is clearer in the conditionally averaged profile of HR shown in Fig. 20.

As the flame approaches extinction by increasing swirl, the heat release rate at negative curvatures drops, but remains unchanged at positive curvatures (Fig. 19d, Fig. 20). The same also occurs when forcing is used (Fig. 19b) and when the velocity is high (Fig. 19c). It is evident that the expected behavior of HR, monotonically decreasing as curvature increases, is captured only for positive curvatures and for flames far from extinction. For flames close to global extinction, it is possible that localized extinctions occur at negative curvatures. The presence of localized extinction is consistent with Fig. 21, which shows the flames located on the modified Borghi diagram described by Lipatnikov and Chomiak [45]. The unforced flame (flame 1) is subject to turbulence which wrinkles and stretches the flame front and is located in the moderate turbulence regime. However, in the highly turbulent flames (flame 3 and flame 4), the flame front is in the flamelet quenching region, resulting in the decreased heat release rates observed in Fig. 20.

4. Conclusions

The application of a diagnostic scheme using the product of OH and CH_2O PLIF images to obtain an image that correlated with the flame heat release rate (HR) was described, and the results were compared with OH^* chemiluminescence measurements. The HR diagnostic provides instantaneous spatially resolved measurements, while the OH^* chemiluminescence is a line-of-sight technique. These diagnostic techniques were compared in turbulent premixed counterflow flames with different bulk strain rates and in forced and unforced bluff-body stabilized flames with different equivalence ratios. In the counterflow flames, the OH^* chemiluminescence and HR techniques showed similar behavior when the strain rate was varied. In the bluff-body flames, the dependence of OH^* chemiluminescence on equivalence ratio was significantly different for the two regions of the flame brush that were considered. The HR measurements were significantly less dependent on the

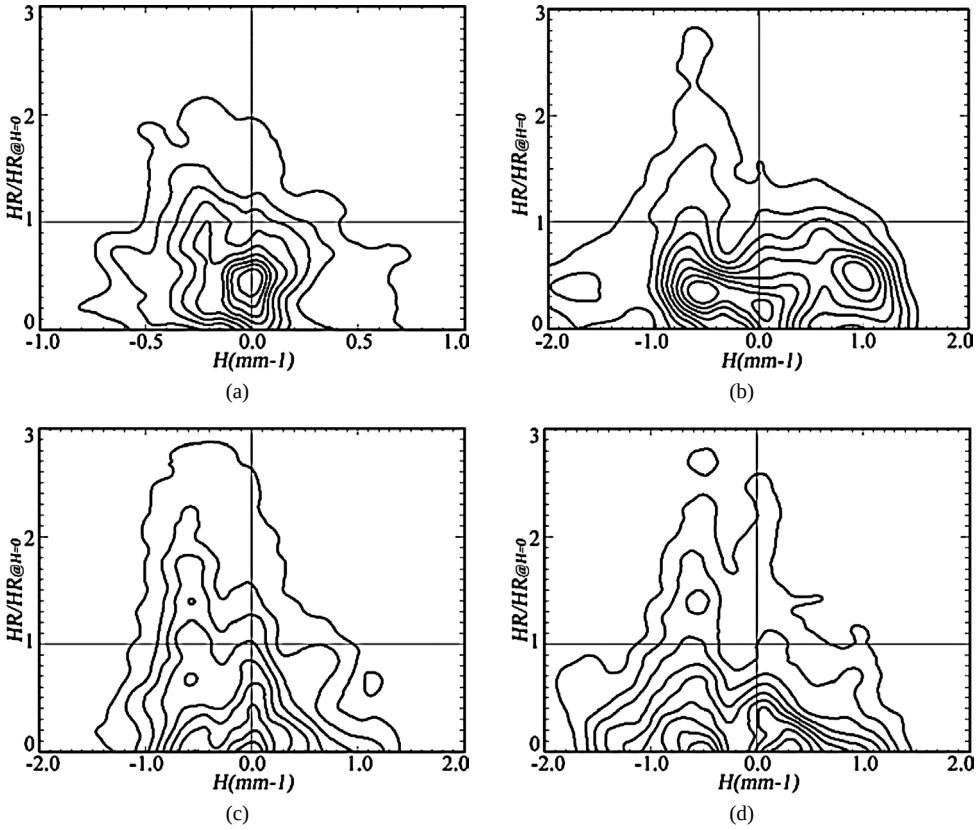

Fig. 19. Contour plots of the joint pdf of HR and curvature for the bluff-body stabilized flames described in Table 1. (a) Flame 1, unforced flame; (b) flame 2, forced flame; (c) flame 3, high velocity and close to extinction; and (d) flame 4, high swirl and close to extinction.

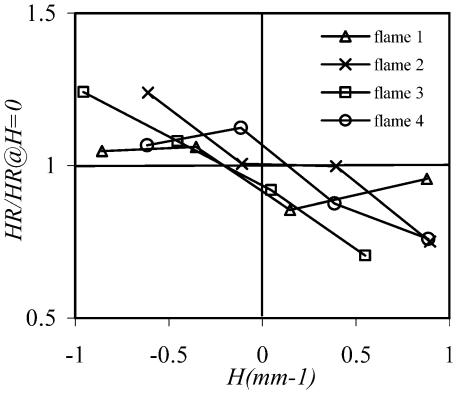

Fig. 20. Average profiles of HR against curvature for the bluff-body stabilized flames described in Table 1. Flame 1, unforced flame; flame 2, forced flame; flame 3, high velocity and close to extinction; and flame 4, high swirl and close to extinction.

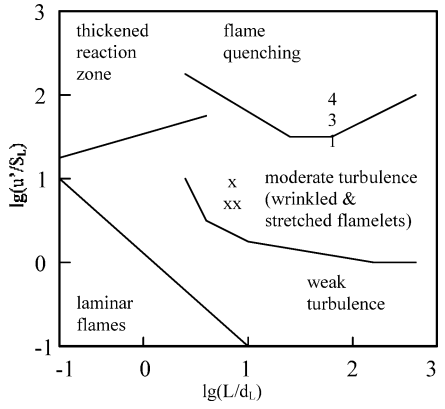

Fig. 21. Modified Borghi diagram describing the turbulence regime of the flames investigated. "x," counterflow flame; 1 (flame 1), unforced flame; 3 (flame 3), high velocity and close to extinction; and 4 (flame 4), high swirl and close to extinction.

location within the flame. These results suggest that OH^* chemiluminescence is more sensitive to variations in turbulence levels and strain rates than the HR measurements.

The correlation of heat release rate and curvature was investigated using the instantaneous heat release rate images obtained with HR in the counterflow

flames and from the bluff-body stabilized flames under different operating conditions. At low bulk velocities, contour plots from the counterflow flames show a bimodal distribution with high HR at negative and positive curvatures, but the trend becomes monotonic at high bulk velocities. The contour plots from the bluff-body stabilized flame show an increase in heat release rate with negative curvatures and a decrease in heat release rate with positive curvatures. This is fully consistent with our expectations from previous results for Le > 1 flames. For flames closer to lean blowout, the correlation is more pronounced, indicating that flames are more sensitive to changes in strain and curvature and could also extinguish locally.

The combined OH and CH_2O PLIF diagnostic provides instantaneous measurements of relative heat release rates in turbulent premixed flames by probing a reaction rate that is highly correlated with heat release. This spatially resolved diagnostic technique enables the structural analysis of instantaneous flame fronts. Although this method is technically and experimentally demanding, it is the closest nonintrusive measure of instantaneous heat release rates that is currently available, and it is therefore a very useful diagnostic tool in combustion research.

Acknowledgments

The authors acknowledge financial support from the Cambridge Commonwealth Trust, the DTI/Rolls Royce collaboration, and the EPSRC under JREI Grant GR/R61994/01 and a PLATFORM grant. We also gratefully acknowledge the support of the Hopkinson Laboratory workshop at the University of Cambridge Engineering Department. J.H. Frank also acknowledges support from the U.S. Department of Energy, Office of Basic Energy Sciences, Division of Chemical Sciences, Geosciences, and Biosciences.

References

[1] A.G. Gaydon, H.G. Wolfhard, Flames: Their Structure, Radiation and Temperature, third ed., Chapman & Hall, London, 1979.
[2] J.G. Lee, D.A. Santavicca, J. Propuls. Power 19 (2003) 735–750.
[3] L.C. Haber, U. Vandsburger, W.R. Saunders, V.K. Khanna, Proc. Int. Gas Turb. Inst. (2000), 2000-GT-0121.
[4] T. Lieuwen, Y. Neumeier, Proc. Combust. Inst. 29 (2002) 99–105.
[5] G.J. Bloxsidge, A.P. Dowling, P.J. Langhorne, J. Fluid Mech. 193 (1988) 445–473.
[6] J.M. Samaniego, F.N. Egolfopoulos, C.T. Bowman, Combust. Sci. Technol. 109 (1995) 183–203.
[7] H.N. Najm, P.H. Paul, C.J. Mueller, P.S. Wyckoff, Combust. Flame 113 (1998) 312–332.
[8] P.H. Paul, H.N. Najm, Proc. Combust. Inst. 27 (1998) 43–50.
[9] C.M. Vagelopoulos, J.H. Frank, Proc. Combust. Inst. 30 (2004) 241–249.
[10] A. Fayoux, K. Zähringer, O. Gicquel, J.C. Rolon, Proc. Combust. Inst. 30 (2004) 251–257.
[11] S. Böckle, J. Kazenwadel, T. Kunzelmann, D.-I. Shin, C. Schulz, J. Wolfrum, Proc. Combust. Inst. 28 (2000) 279–286.
[12] A.P. Dowling, Aeronaut. J. 104 (2000) 105–116.
[13] R. Balachandran, B.O. Ayoola, C.F. Kaminski, A.P. Dowling, E. Mastorakos, Combust. Flame (2005), in press.
[14] C.A. Armitage, A.J. Riley, R.S. Cant, A.P. Dowling, S.R. Stow, Proc. ASME Turb. Expo. (2004), 2004-GT-53820.
[15] S.-H. Lee, I.-C. Chen, J. Chem. Phys. 105 (1996) 2583–2590.
[16] J.B. Jeffries, D.R. Crosley, I.J. Wysong, G.P. Smith, Proc. Combust. Inst. 23 (1990) 1847–1854.
[17] J.E. Rehm, P.H. Paul, Proc. Combust. Inst. 28 (2000) 1775–1782.
[18] J.H. Frank, S.A. Kaiser, M.B. Long, Proc. Combust. Inst. 29 (2002) 2687–2694.
[19] The San Diego Mechanism, Center for Energy Research, University of California at San Diego, 2003, available at: http://maemail.ucsd.edu/combustion/cermech/.
[20] P.H. Paul, J. Quant. Spectrosc. Radiat. Transfer 51 (3) (1994) 511–524.
[21] M. Tamura, P.A. Berg, J.E. Harrington, J. Luque, J.B. Jeffries, G.P. Smith, D.R. Crosley, Combust. Flame 114 (1998) 502–514.
[22] C.K. Law, C.J. Sung, G. Yu, R.L. Axelbaum, Combust. Flame 98 (1994) 139–154.
[23] S.D. Lee, S.H. Chung, Combust. Flame 98 (1994) 80–92.
[24] J.A. van Oijen, L.P.H. de Goey, Combust. Theory Modelling 6 (2002) 463–478.
[25] R.P. Lindstedt, D. Luff, D. Smith, J.H. Whitelaw, in: 12th International Symposium on the Application of Laser Techniques to Fluid Mechanics, 2004, paper 13-1.
[26] E. Mastorakos, A.M.K.P. Taylor, J.H. Whitelaw, Combust. Flame 91 (1992) 40–54.
[27] L.W. Kostiuk, K.N.C. Bray, R.K. Cheng, Combust. Flame 92 (1993) 396–409.
[28] Y. Hardalupas, M. Orain, C.S. Panoutsos, A.M.K.P. Taylor, J. Olofsson, H. Seyfried, M. Richter, J. Hult, M. Aldén, in: 1st International Conference on Gas Turbine Technologies, Brussels, 2003.
[29] K. Jambunathan, X.Y. Ju, B.N. Dobbins, S. Ashforth-Frost, Meas. Sci. Technol. 6 (1995) 507–514.
[30] K.T. Walsh, J. Fielding, M.B. Long, Opt. Lett. 25 (2000) 457–459.
[31] S.R. Turns, An Introduction to Combustion, second ed., McGraw–Hill, New York, 2000.
[32] K.N.C. Bray, M. Champion, P.A. Libby, Combust. Flame 107 (1996) 53–64.
[33] S. Ishizuka, C.K. Law, Proc. Combust. Inst. 19 (1982) 327–335.

[34] D. Luff, E. Korusoy, P. Lindstedt, J.H. Whitelaw, Exp. Fluids 35 (2003) 618–626.
[35] D. Veynante, J. Piana, J.M. Duclos, C. Martel, Proc. Combust. Inst. 26 (1996) 413–420.
[36] K.N.C. Bray, R.S. Cant, Proc. R. Soc. London Ser. A 434 (1991) 217–240.
[37] M.Z. Haq, C.G.W. Sheppard, R. Woolley, D.A. Greenhalgh, R.D. Lockett, Combust. Flame 131 (2002) 1–15.
[38] T.W. Lee, G.L. North, D.A. Santavicca, Combust. Flame 93 (1993) 445–456.
[39] T.C. Chew, K.N.C. Bray, R.E. Britter, Combust. Flame 80 (1990) 65–82.
[40] L.W. Kostiuk, I.G. Shepherd, K.N.C. Bray, Combust. Flame 118 (1999) 129–139.
[41] T. Echekki, J.H. Chen, Combust. Flame 106 (1996) 184–202.
[42] C.J. Rutland, A. Trouvé, Combust. Flame 94 (1993) 41–57.
[43] M. Tanahashi, Y. Nada, Y. Ito, T. Miyauchi, Proc. Combust. Inst. 29 (2002) 2041–2049.
[44] S. Gashi, J. Hult, K.W. Jenkins, N. Chakraborty, R.S. Cant, C.F. Kaminski, Proc. Combust. Inst. 30 (2004) 809–817.
[45] A.N. Lipatnikov, J. Chomiak, Prog. Energy Combust. Sci. 28 (2002) 1–74.